Converted-wave prestack depth imaging with the nonstationary wavefield extrapolators

Yanpeng Mi and Gary F. Margrave

ABSTRACT

The PSPI dual extrapolation algorithm is applied to converted-wave prestack depth imaging. The 1997 Blackfoot 3C-2D data is used for the testing purpose. Both the P-P and P-S data were migrated and compared. The resulting P-P and P-S reflectivity images are very clear, except for edge effects, and they tie reasonably well in depth.

INTRODUCTION

Shear-wave exploration has certain advantages over conventional P wave methods. Since shear-wave velocity depends only on the rock matrix structure, it is more able to penetrate gas-rich strata to obtain better reflection signal. However; shear-wave sources often have less energy and lower dominant frequencies compared with conventional acoustic sources. The inclusion of horizontal components with conventional vertical-component recording leads to inexpensive acquisition of valuable mode-converted shear-wave (P-S) data with a conventional seismic source. Converted shear-wave reflections (P-S) have smaller reflection angles than P wave reflections so that more information can be acquired in the same aperture. Shear waves converted from incident P waves allow estimation of the elastic parameters of the subsurface, which are important in many aspects of reservoir exploration, characterization and exploitation.

The major complexity in processing P-S data is the asymmetry of the source-to-receiver raypaths. Conventional common-midpoint (CMP) based processing techniques cannot be used. Birefringence analysis (Harrison, 1993), common-conversion-point (CCP) binning, P-S NMO correction and velocity analysis (Slotboom et al., 1989, 1990), P-S DMO and migration (Eaton and Stewart, 1991 and Harrison, 1993), are required. There has been an increased utilization of P-S waves in anisotropy analysis (Thomson, 1999; Bale et al., 1998). Depth migration of P-S data for sub-salt imaging and in anisotropic media has been discussed by several authors (Sekulic and Gaiser, 1998, Agosto et al., 1998, Caldwell et al., 1998, Sollid et al., 1996). True-amplitude prestack imaging of P-S data has also been discussed (for example, Nicoletis et al., 1998). Extended from land 3-C acquisition technology, ocean-bottom-cable acquisition, which consists of 3-C geophones and hydrophones, can directly record P-S data at the ocean bottom and this technology has many advantages over marine acoustic surveys. The processing difficulties brought by ocean-bottom-multiples can be better more delicately handled by utilizing the pressure data recorded by hydrophones.

Converted-wave data acquired over complex geology presents great challenges for conventional P-S processing algorithms such as CCP binning, P-S DMO and migration. These conventional algorithms are first reviewed in this paper. The theory of elastic wave extrapolation is then reviewed. It will be shown that the Fourier-

domain wavefield-extrapolation theory, which has been very successful in handling P-wave data, can be conveniently applied to converted-wave prestack depth imaging. Data from the 1997 Blackfoot 3C-3D survey is used to demonstrate this.

CONVENTIONAL CONVERTED WAVE PROCESSING

Figure 1 shows a routine P-S processing flow (Harrison, 1993). The vertical component data is often processed before P-S processing to provide initial velocity information and source statics. For 2-D split-spread acquisition geometry, the recorded radial component on both sides of the source has reversed polarity. Data on either side of the source, normally the trailing spread, needs to be polarity-reversed so that stacking processing doesn't destroy events.

Common-conversion-point (CCP) binning is an important step in P-S data processing. It is well known that the lateral position of a conversion point varies with depth when the offset is constant (Chung and Corrigan, 1985; Tessmer and Behle, 1988; Eaton et al., 1990). For small offset/depth ratios, the asymptotic CCP binning approximation is usually good enough. A more accurate way of CCP binning is the depth-variant binning algorithm (Tessmer and Behle, 1988; Eaton et al., 1990).

For flat reflections, the P-S moveout curves are hyperbolic to the first order (Tessmer and Behle, 1988) and standard velocity analysis tools can still be used to obtain a stacking velocity function (Taner and Koehler, 1969). With P-wave velocity obtained from the conventional P-P data, the shear-wave velocity can be calculated.

P-S dip-moveout correction (P-S DMO) is appropriate in regions of complex structure to reduce the destructive interference caused by dipping events (Deregowski and Rocca, 1981). The algorithm is more complicated than the conventional P-P DMO; Harrison (1993) gives a complete description.

A P-S stacked section can be migrated to improve focusing. The time coordinate of a zero-offset P-S stack section is the zero-offset travel time with P wave down and S wave up. The P-S diffraction curves on a zero-offset P-S section are approximately hyperbolic to first order (Harrison, 1992) and this means that the migration can be done in a fashion similar to conventional P-P zero-offset migration.

Many authors have recently addressed prestack migration and migration-velocity analysis of P-S data. Most approaches are Kirchhoff summation algorithms similar to conventional P-P algorithms. A P-S raytracing instead of P-P raytracing is carried out to compute the traveltime curve. Samples along a traveltime curve are then scaled by amplitude correction factors and then summed. In complex media, the difficulties encountered in P-P raytracing, for example, chaotic rays, are more likely to happen in P-S raytracing since the P-S velocity contrast is normally larger than P-P velocity contrast. Fourier-domain imaging techniques, which have many advantages in the P-P cases, should have similar advantages in the P-S case, especially in complex media.

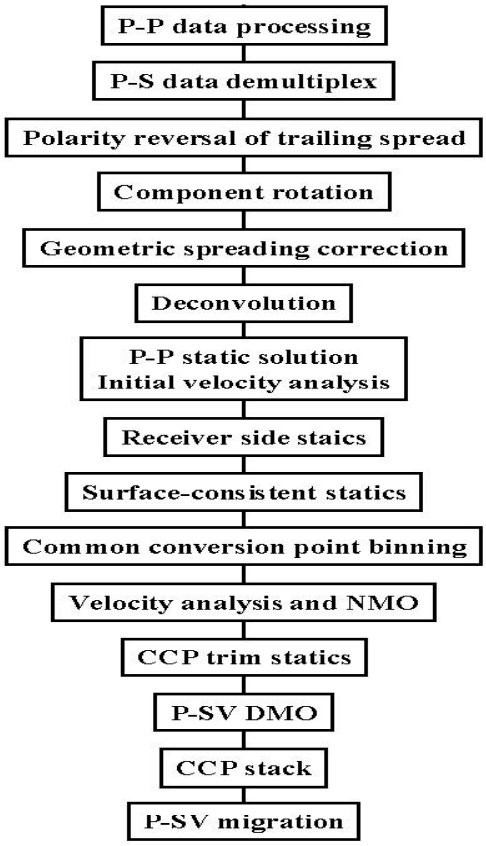

FIG. 1. Conventional P-S data processing flow (Harrison, 1993).

P-S WAVE REFLECTION AT A SOLID-SOLID BOUNDARY

Consider P- and SV-incident wavefields impinging on a solid-solid boundary between two isotropic homogeneous media in welded contact. The parameters describing each of the media are α_j, β_j, ρ_j, λ_j and μ_j, where j=1 corresponds to the upper media and j=2 corresponds to the lower media. α_j, β_j, ρ_j are P-wave velocity, S-wave velocity and density, respectively. λ_j and μ_j are Lamé elastic parameters. The wavefields occuring at the boundary as the results of an incident elastic wave train are shown in Figure 2. A mathematical description of these wave modes can be found in many elastic wavefield propagation texts (for example, Aki and Richards, 1980).

Acoustic-wavefield extrapolation is a simplification of the elastic-wave propagation theory that ignores the shear wavefield. By further ignoring the multiple wavefield, the recorded primaries-only acoustic wavefield can be expressed with the ***WRW*** model (Berkhout, 1980). The primaries-only converted-wave reflection can be expressed in a similar way. Let $\boldsymbol{W_P}$ stand for the down-going P wavefield propagator, $\boldsymbol{C}$ stands for the P to SV conversion coefficients and $\boldsymbol{W_S}$ stand for the primary up-going S wavefield propagators, the physical process of P-S conversion can then be expressed as a $\boldsymbol{W_P C W_S}$ model (Figure 3).

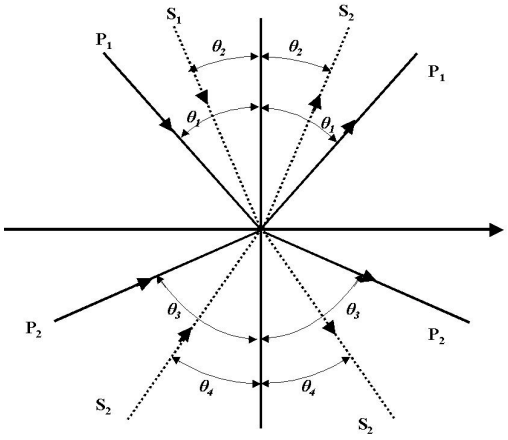

Fig. 2. Incidence of a P or SV wave from medium 1 or medium 2. The angles θ_i, (i=1, 2, 3, 4) are related to the ray parameter or horizontal slowness p by the relation $p = \sin\theta_1 / \alpha_1$, $p = \sin\theta_2 / \beta_1$, $p = \sin\theta_3 / \alpha_2$ and $p = \sin\theta_4 / \beta_2$.

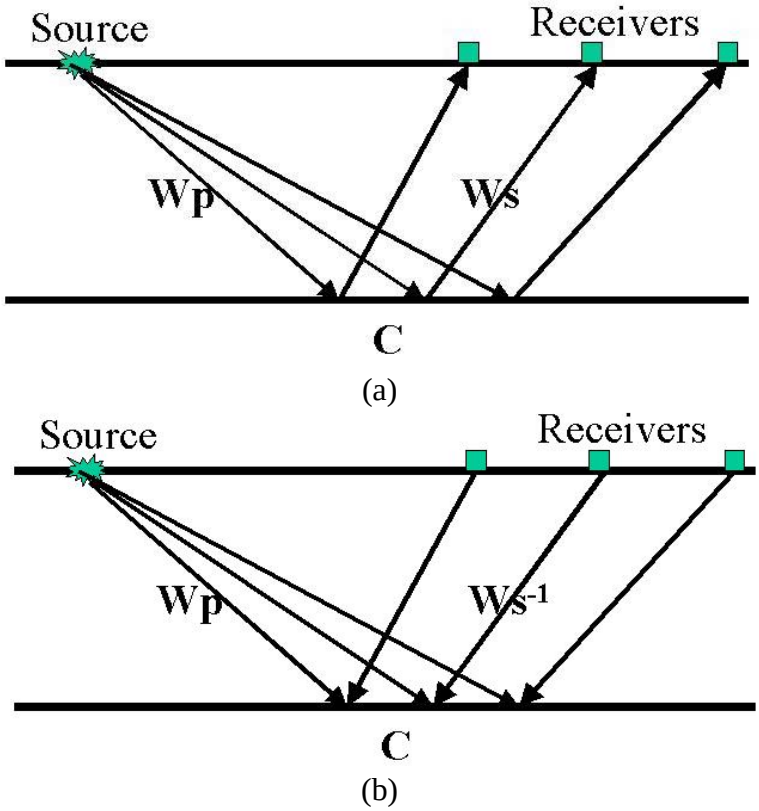

Figure 3. (a) The ***$W_P C W_S$*** model for converted-wave reflection for a horizontal boundary; (b) Depth imaging of the boundary involves forward extrapolation of the source signature and inverse extrapolation of the recorded primary-only P-S data.

A converted-wave imaging condition can be expressed in a form similar to the P-P imaging condition. For a monochromatic plane wave, at any particular depth, the P-S reflection coefficient at a boundary can be expressed as the ratio between the S

wavefield immediately after conversion and the P wavefield immediately before hitting the boundary. An average of all the frequency-dependent conversion coefficients is computed to avoid frequency-dependency. The conversion coefficients can be written as,

$$\tilde{r}(\mathrm{x},z)=\frac{1}{[\omega_{\max}-\omega_{\min}]}\int_{\omega_{\min}}^{\omega_{\max}}\left\{\frac{\psi^{*}_{C}(\mathrm{x},z,\omega)}{\psi^{*}_{P}(\mathrm{x},z,\omega)}+\frac{\psi_{C}(\mathrm{x},z,\omega)}{\psi_{P}(\mathrm{x},z,\omega)}\right\}d\omega . \qquad (2.8)$$

where ψ_C and ψ_P are the converted shear wavefield and the incident P wavefield, and * denotes complex conjugation.

THE 1997 BLACKFOOT 3C-2D SURVEY

The Blackfoot 3C-2D high-resolution survey was conducted in 1997 as a joint effort between the CREWES project at the University of Calgary and Boyd PetroSearch Consultant Ltd. and PanCanadian Petroleum ltd. The Blackfoot field is located about 50-55Km east of Calgary near the town of Strathmore, Alberta (Figure 4). The producing formation is Lower Cretaceous, cemented glauconitic sand, which was deposited as incised channel-fill sediment above the Mississippian carbonates. The glauconitic sandstone lies at depth of about 1,500m below surface and is up to 45m thick. The average porosity in this producing unit is about 18%. Figure 5 shows a sedimentary sequence of southern Alberta and the blocked P and S velocity measured from well 0908 that is located roughly in the middle of the 3C-2D line which as acquired in 1997. The cumulative production from it throughout southern Alberta exceeds 200MMbls oil and 400BCF gas (Miller et al., 1995). Figure 6 shows an isopach of the reservoir and the locations of the wells and the 1997 2D-3C survey.

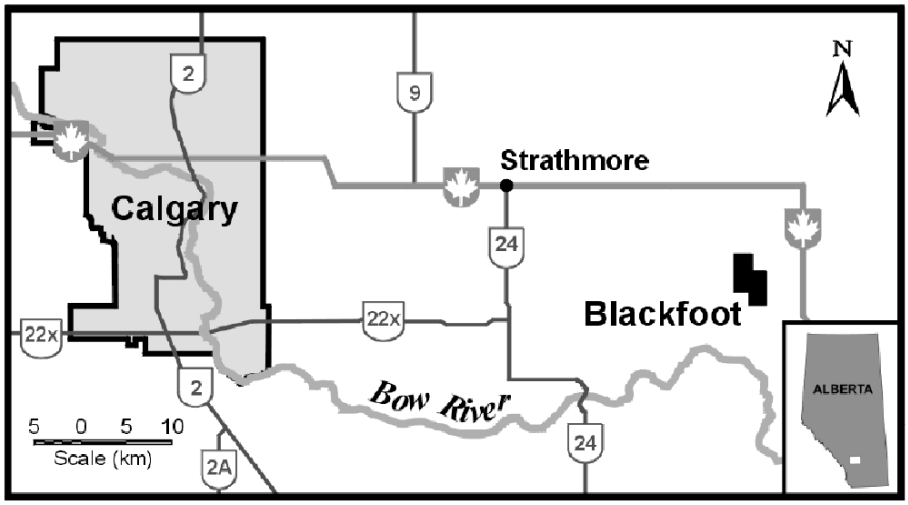

FIG. 4. Map showing the location of the Blackfoot field where the high-resolution 3C-2D seismic survey was conducted.

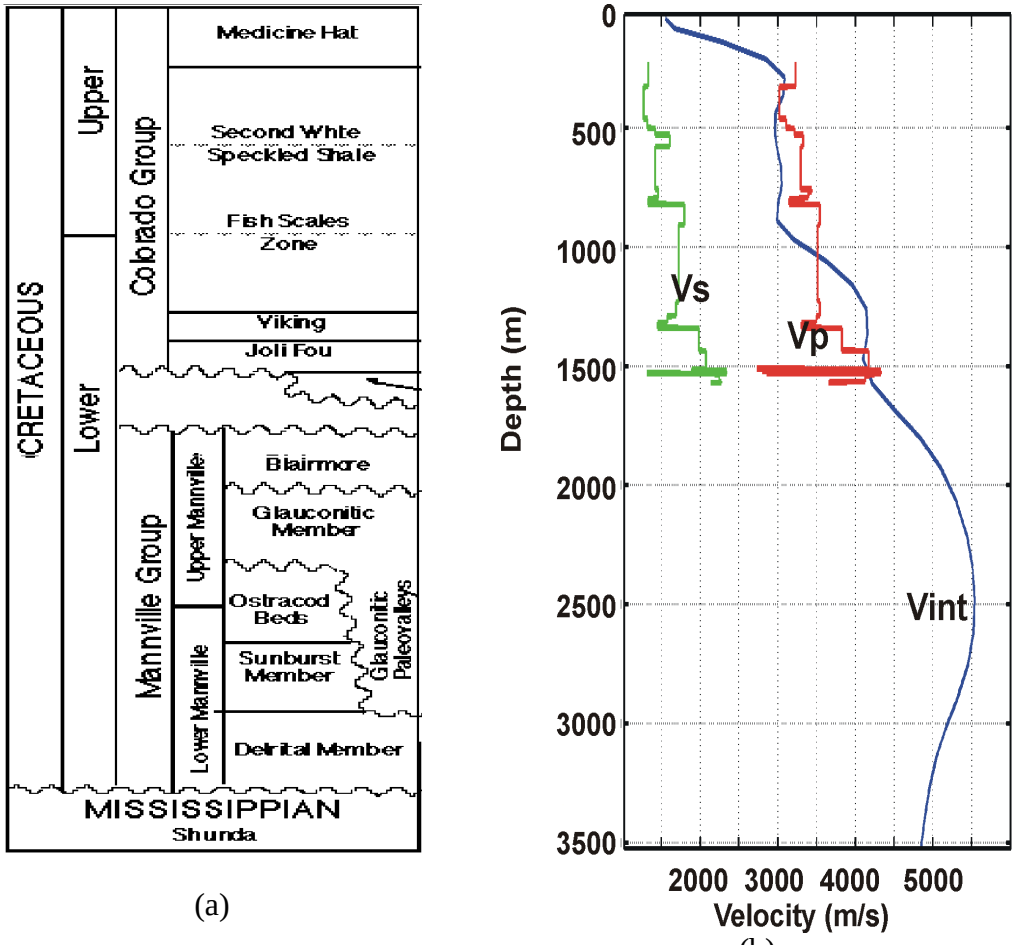

FIG. 5. The sedimentary sequence of southern Alberta (a) and the blocked Vp and Vs from well l0908. Light grey and dark grey solid lines are the Vs and Vp, respectively. Interval velocity computed from seismic velocity analysis of the P-wave data is also shown as a black solid line in (b).

The survey involved acquisition of a 3km 3C-2D-reflection profile that consisted of combination of conventional and high-resolution receiver intervals. Figure 6 is also the acquisition base map in the region. Figure 7 shows a schematic diagram of the acquisition geometry. The source interval employed for the entire 2-D profile was 20m with source-positions on the half station. The survey also involved simultaneous recording into 21x3 buried 3-C geophones situated in 6-, 12- and 18-m holes drilled every 50m along the central kilometre of the profile. In addition to these buried geophones, a 48-channel vertical hydrophone cable with a 2m receiver interval was deployed in a 100m cased hole located in the centre of the profile. A walk-away VSP was also simultaneously recorded in PanCanadian's 100/09-08-23-23W4 well, located near the centre of the spread, by recording the full range of offsets for each tool position.

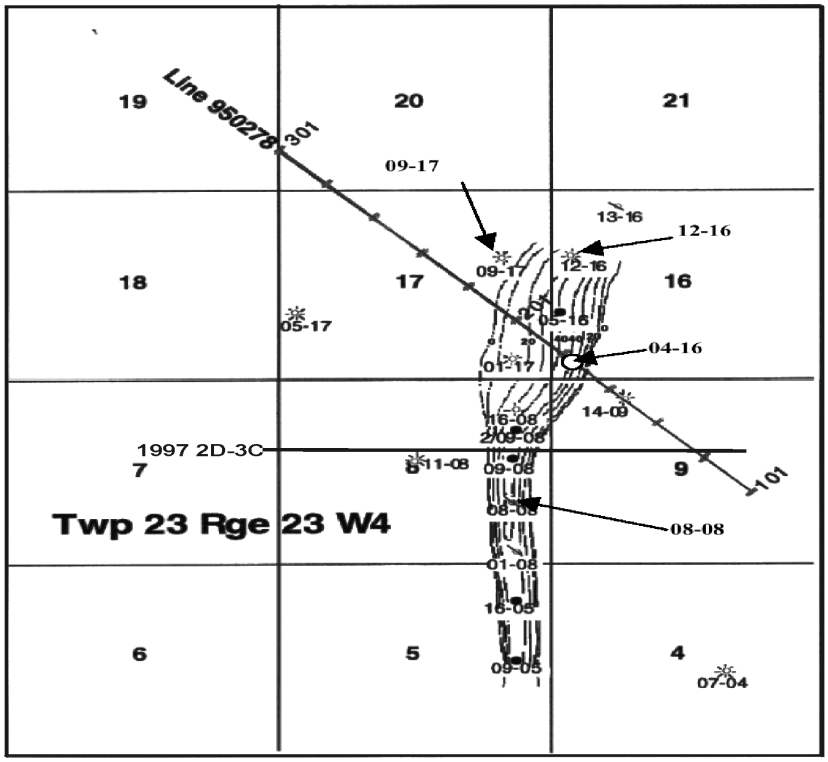

FIG. 6. Isopach of the Blackfoot Galuconitic incised valley. The dashed line is the isopach and the contour interval is 10 m. The 1997 3C-2D line roughly perpendicular to the glauconite channel. Line 950728 was shot in 1995.

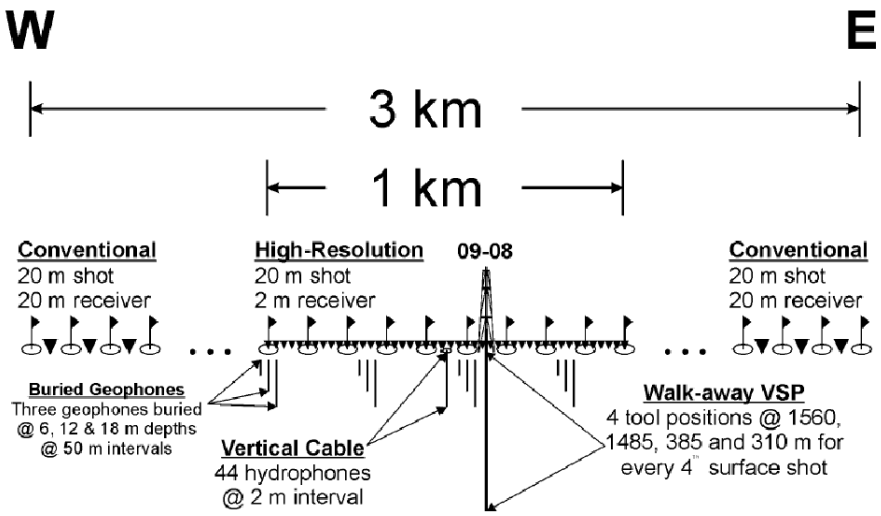

FIG. 7. Acquisition geometry of the 1997 Blackfoot survey.

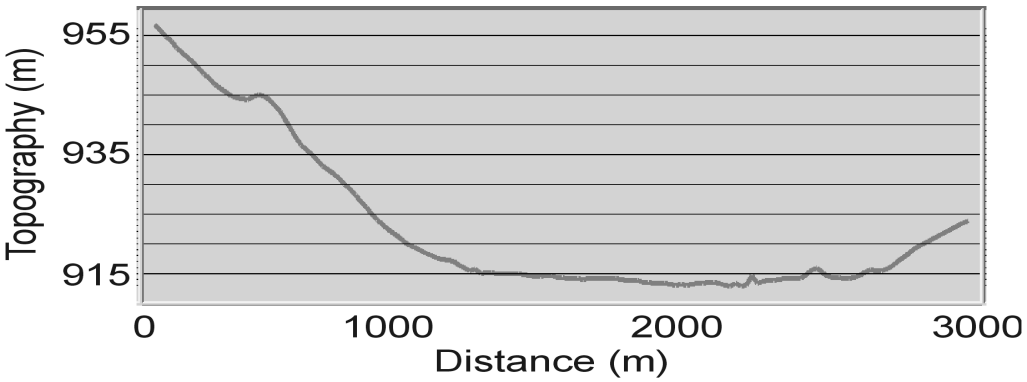

FIG. 8. Topography variation across the line.

Topography variation across the line is rather mild. The elevation difference between the highest point (west of the line) and the lowest point (roughly around 2100 m from the left end of the line) is only about 40 m (Figure 8|). However, considering the low near-surface velocity and that Vs is normally much slower than Vp, the receiver elevation statics are often large enough to degrade stacking. Migration from topography is thus indicated for converted-wave prestack depth imaging.

PRESTACK DEPTH IMAGING THE VERTICAL AND RADIAL COMPONENT

Velocity model

The 3C-2D line acquired in 1997 was previously processed by Cieslewicz and Lawton (1998) and several issues were discussed. Since the geology in Blackfoot region lacks structural deformation and the strata are almost flat, a V(z) velocity function should give a fairly good approximation in the velocity field across the line. The log from well 0908, which is located roughly in the middle of the line, is used to determine the V(z) function. Since the well log ran from about 220m below the topography to the depth of 1560m, the P-wave velocity function from the surface to 200m and the velocity below 1560m is approximated with the interval velocity computed from the stacking velocity from P-P velocity analysis. The S-wave velocity function outside of the logging interval, however, is determined from a statistical relationship between the Vp and Vs within the logging interval. Figure 9 shows the Vp-Vs cross-plots from the well 0908. Note the cross-plot of all the overall logging interval shows that there are two Vp-Vs variation trends. The dominant trend, as plotted with black solid line can be written as

$$Vs = 0.9286Vp - 1592.9 \quad , \tag{5}$$

where the Vp and Vs are in m/s. The secondary trend that Vs does not change much while Vp increases dramtically, as highlighted with ellipses, only appears in the shallow part of the well log. To illustrate this, the well log is devided into four intervals, 220m to 550m, 550m to 900m, 900m to 1250m and 1250m to 1560m and the Vp-Vs cross-plots are also shown in Figure 9. Note this secondary trend

disappears below 900m. The S-wave velocity model outside of the logging interval is then can be computed from the interval velocity as shown in Figure 5.

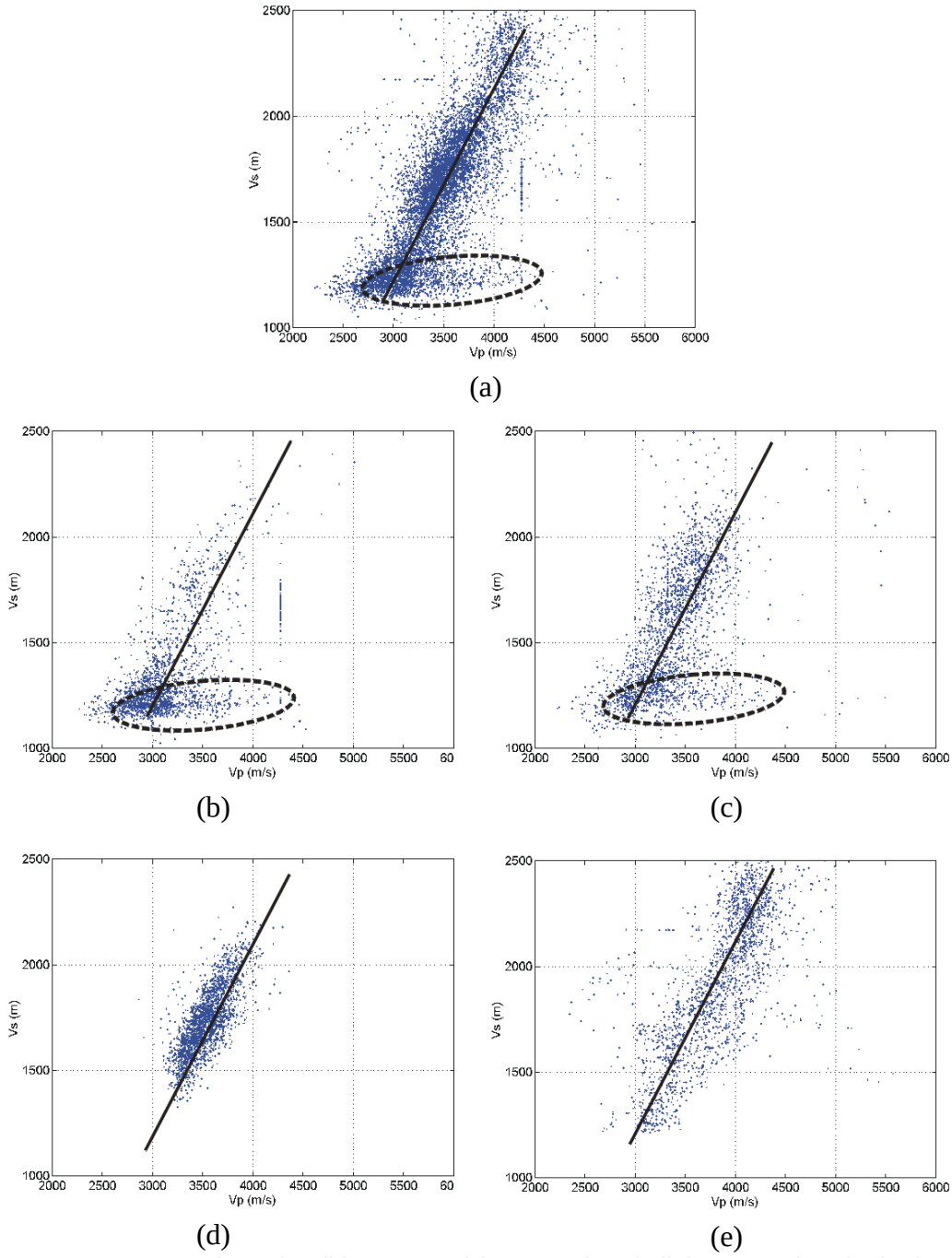

FIG. 9. Vp-Vs cross-plots of well log 09-08. (a) Cross-plot of all the Vp and Vs in the logging interval; (b) Cross-plot of the interval from 220m to 550m.; (c) Cross-plot of the interval from 550m to 900m; (d) Cross-plot of the interval from 900m to 1250m; (e) Cross-plot of the interval from 1250m to 1560m. The black solid lines are the dominant Vp-Vs relationship. Dashed line ellipse highlights the erroneous measurements.

Figure 10 shows the V_p and V_s depth model built with both the well log and the seismic interval velocity. They are mainly *V(z)* media except that the velocities are

interpolated from 220m below the well head elevation to the topography using the Vp-Vs relationship discussed above.

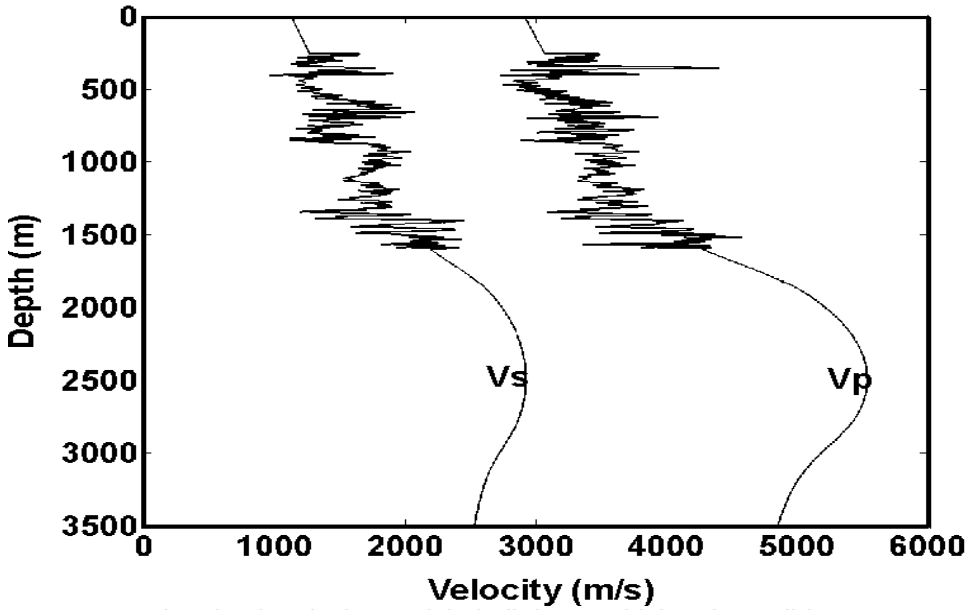

Figure 10. P and S depth-velocity models built by combining the well log measurement, the interval seismic velocity and the statistical relationship of equation 5. Solid white lines are the topography.

Preprocessing

The vertical component has a good S/N ratio. Figure 12(a) shows the shot 75, which is located in the middle of the line. A surface-consistent deconvolution was first applied to remove both the source wavelet and the receiver response. A forward shot-gather normal-moveout correction was applied to flatten the events so that an FK filter could be applied to remove most of the ground-roll energy. A time-variant spectral whitening was also applied to further enhance vertical resolution, especially that of the deep events. A surface-consistent residual statics correction was applied to enhance the event coherency. The long-wavelength component statics were removed after residual statics were applied. The data after the above processing can be seen in Figure 14.

For P-S data, the two horizontal components were rotated to form the radial component. Polarity of the data with negative offset was reversed so that stacking of the data with offsets of opposite signs did not cancel. Figure 12(b) shows the shot gather 75 in the middle of the line. Note the low S/N ratio and low resolution. The signal-processing flow applied to the radial component is roughly the same with parameters adjusted to fit the shear-wave data. Since hand-statics play a crucial role in the data processing, they were picked and applied after application of the shear-wave elevation statics and refraction statics. The statics corrections bring the data to a floating datum that is different from the true surface topography. Migration from the floating datum rather than from the topography was used. Due to the low S/N ratio, an F-X noise reduction was applied after removal of the ground-roll and before

inverse NMO correction. The P-S data after the above processing flow is shown in Figure 15. As a summary, the pre-processing flow for the vertical and the radial component data are shown in Figure 13.

Migration results

A PSPI dual-algorithm with 40m step-size was used for image processing. It took about 30 seconds to migrate a shot gather to a maximum depth of 3500m on an Alpha-XP1000 workstation with 512Mb memory. Figure 14 shows vertical-component shot gathers 10, 75, and 150 after the pre-processing and the corresponding migration results. Figure 15 shows the corresponding radial component shot gathers after the pre-processing and the migration results. Figure 16 shows three vertical components CIGs located at 500m, 1500m, and 2500m of the line and Figure 17 shows the corresponding radial component CIGs. Each of these CIGs is stacked to produce the final P-P depth image (Figure 18) and the P-S depth images (Figure 19). Both images are of high quality except for the strong wavefronting at the section boundaries. With the correct velocity model, these two sections should have high correlation.

CORRELATION OF P-P AND P-S DEPTH IMAGE

It is generally difficult to correlate a P-P time section and a P-S time section with the uncertainty in seismic amplitude and velocity model. The same difficulty also exists in depth section correlation analysis because the prestack depth imaging is more sensitive to velocity errors. The events in Figure 17(a) and (c) still curve up slightly, which indicates the shear velocity model is probably slower than the actual velocity. This can be roughly corrected by slightly increase the shear wave velocity, and a more scientific way is to use migration velocity analysis to obtain more accurate velocity model. Figure 20 shows the correlation analysis of the P-P image and P-S image. The central part of the P-P image is replaced with the P-S image. Note that the shallow part has excellent correlation: for example, the events at 300m, 950m and 1550m, while the events in the deeper part are slightly mis-tied.

CONCLUSIONS

In this paper, the theory of elastic-wave scattering at a solid-solid boundary is reviewed. A simplification of this provides the theoretical foundation of for wavefield extrapolation and converted-wave imaging by considering only the downgoing P wavefield and up-going S wavefield. The resulting WCW wave-propagation model for converted-wave imaging is proposed. Automatic common-conversion-point (CCP) binning occurs in each step of the wavefield extrapolation so that the algorithm is adaptable to P/S ratios varying in both the vertical and horizontal directions. The algorithm is superior to the raytracing-based CCP binning with a single P/S ratio and is suitable for regions of complex geology.

The 1997 Blackfoot 2-D line was used for algorithm testing. A spatial phase-shift algorithm to adjust source position in order to handle source geometry irregularity is discussed. Both the well log from well 0908 and the interval velocity obtained from the stacking velocities were used to build the velocity model. Due to their different

statics corrections, the vertical-component data was migrated from the topography, while the radial-component was migrated from the floating datum produced by the statics corrections. The P-P depth image quality is rather satisfying while the P-S depth image quality is slightly inferior. This may be due to poor S/N ratio in the original data and errors in the velocity model. The shallow part of the two depth-sections shows good correlation while the deeper parts are slightly mistied.

ACKNOWLEDGEMENTS

We appreciate the support of CREWES sponsors and NSERC, which was essential to this work.

REFERENCES

Aki, K., and Richards, P.G., 1980, Quantitative seismology V1, W.H. Freeman and Company.

Bale, R.A., Farmer, P., Hansen, J. O., Nichols, D.E., and Palacharla, G. K., 1998, Prestack depth migration of converted wave data in anisotropic media, 68th Ann. Internat. Mtg: Soc. Of Expl. Geophys., 1108-1111.

Caldwell, J., Kristiansen, P., Beaudoin, G.J., Tollestrup, A.K., Siddiqui, S.A., Wyatt, K., Camp, W. and Raney, G.B., 1998, Marine 4-component seismic test, Gulf of Mexico: Subsalt Imaging at Mahogany Field: Annual Meeting Abstracts, Society Of Exploration Geophysicists, 2091-2092.

Caldwell, J., Kristiansen, P., Beaudoin, G.J., Tollestrup, A.K., Siddiqui, S.A., Chauris, H., Lambare, G., Noble, M., and Podvin, P., 1999, Migration-based velocity analysis in 2-D laterally heterogeneous media, 69th Ann. Internat. Mtg: Soc. of Expl. Geophys., 1235-1238.

Chung, W.Y. and Corrigan, D., 1985, Gathering mode-converted shear waves: A model study, 55th Ann. Internat. Mtg: Soc. Of Expl. Geophys., Session:S18.7.

D'Agosto, C., Donati, M.S. and Michelena, R.J., 1998, Tomography + pre-stack depth migration of P-S converted waves, 68th Ann. Internat. Mtg: Soc. of Expl. Geophys., 1361-1364.

Deregowski, S.M. and Rocca, F., 1981, Geometrical optics and wave theory of constant offset sections in layered media: Geophys. Prosp., Eur. Assn. Geosci. Eng., 29, 374-406.

Eaton, D.W.S., Slotboom, R.T., Stewart, R.R., and Lawton, D.C., 1990, Depth-variant converted-wave stacking, 60th Ann. Internat. Mtg: Soc. of Expl. Geophys., 1107-1110.

Eaton, D.W.S. and Stewart, R.R., 1991, Anisotropic ray-Born migration/inversion: A synthetic modeling study, CREWES Research Report, 1991

Harrison, M.P., 1993, Processing of P-SV Surface-Seismic Data: Anisotropy Analysis, Dip Moveout, and Migration, Ph.D. Thesis, Department of Geology and Geophysics, the University of Calgary.

Nicoletis, L.M., Svay-Lucas, J., and Prigent, H., 1998, True amplitude pre-stack imaging of converted waves: Annual Meeting Abstracts, Society Of Exploration Geophysicists, 734-737.

Sekulic, D.M., Gaiser, J.E., and Albertin, U.K., 1998, Role of salt base converted wave phase shift in subsalt imaging, 68th Ann. Internat. Mtg: Soc. of Expl. Geophys., 582-585.

Slotboom, R.T., 1990, Converted wave (P-SV) moveout estimation, 60th Ann. Internat. Mtg: Soc. of Expl. Geophys., 1104-1106.

Slotboom, R.T. and Lawton, D.C., 1989, Depth-variant mapping and moveout correction of converted-wave data, CREWES Annual Report, 1989

Sollid, A., Ekren, B. O., and Arntsen, B., 1996, Prestack time migration applied to marine P-SV seismic waves, 66th Ann. Internat. Mtg: Soc. of Expl. Geophys., 1571-1574.

Taner, M.T. and Koehler, F., 1969, Velocity spectra - Digital computer derivation and applications of velocity functions : Geophysics, Soc. of Expl. Geophys., 34, 859-881. (* Errata in GEO-36-4-0787)

Tessmer, G. and Behle, A., 1988, Common reflection point data-stacking technique for converted waves: Geophys. Prosp., Eur. Assn. Geosci. Eng., 36, 671-688.

Thomson, L., 1999, Converted-wave reflection seismology over inhomogeneous, anisotropic media: Geophysics, Soc. Of Expl. Geophys., 64, 678-690.

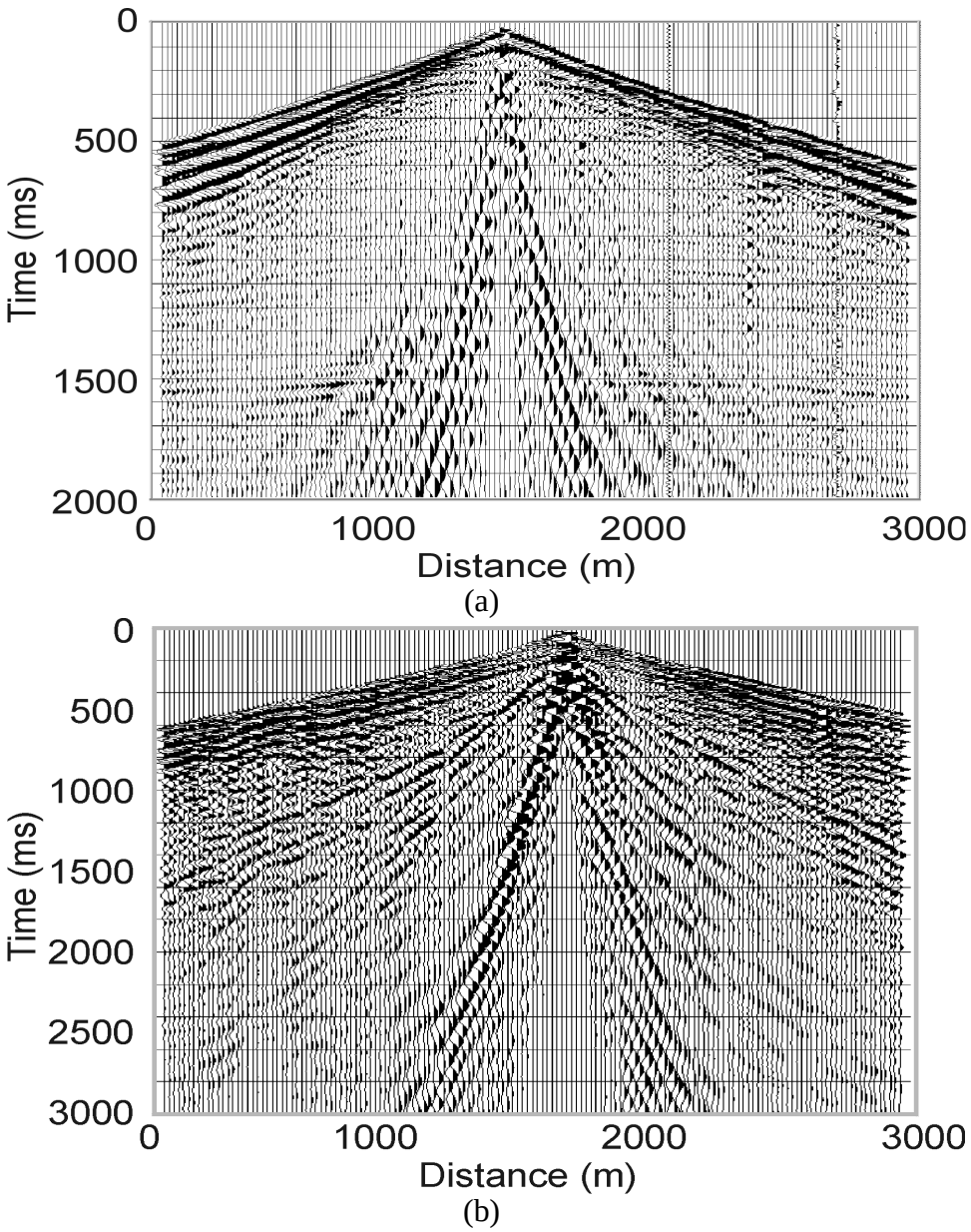

FIG. 12. (a) Vertical component shot gather 75 with 2000ms AGC and (b) radial component shot gather 75 with 1000ms AGC.

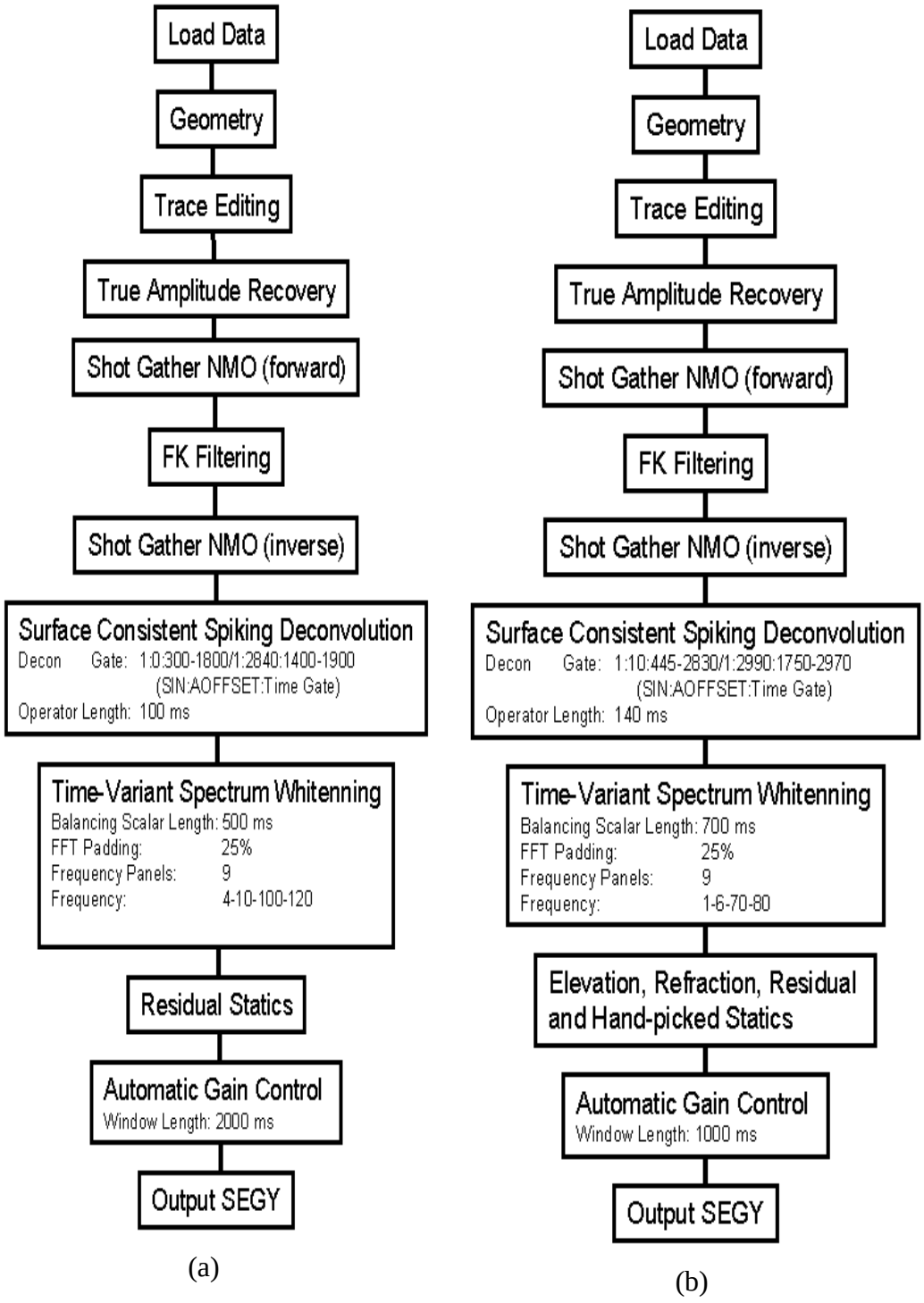

FIG. 13. (a) Pre-processing flow and parameters for the vertical component data and (b) pre-processing flow and parameters for the radial component data.

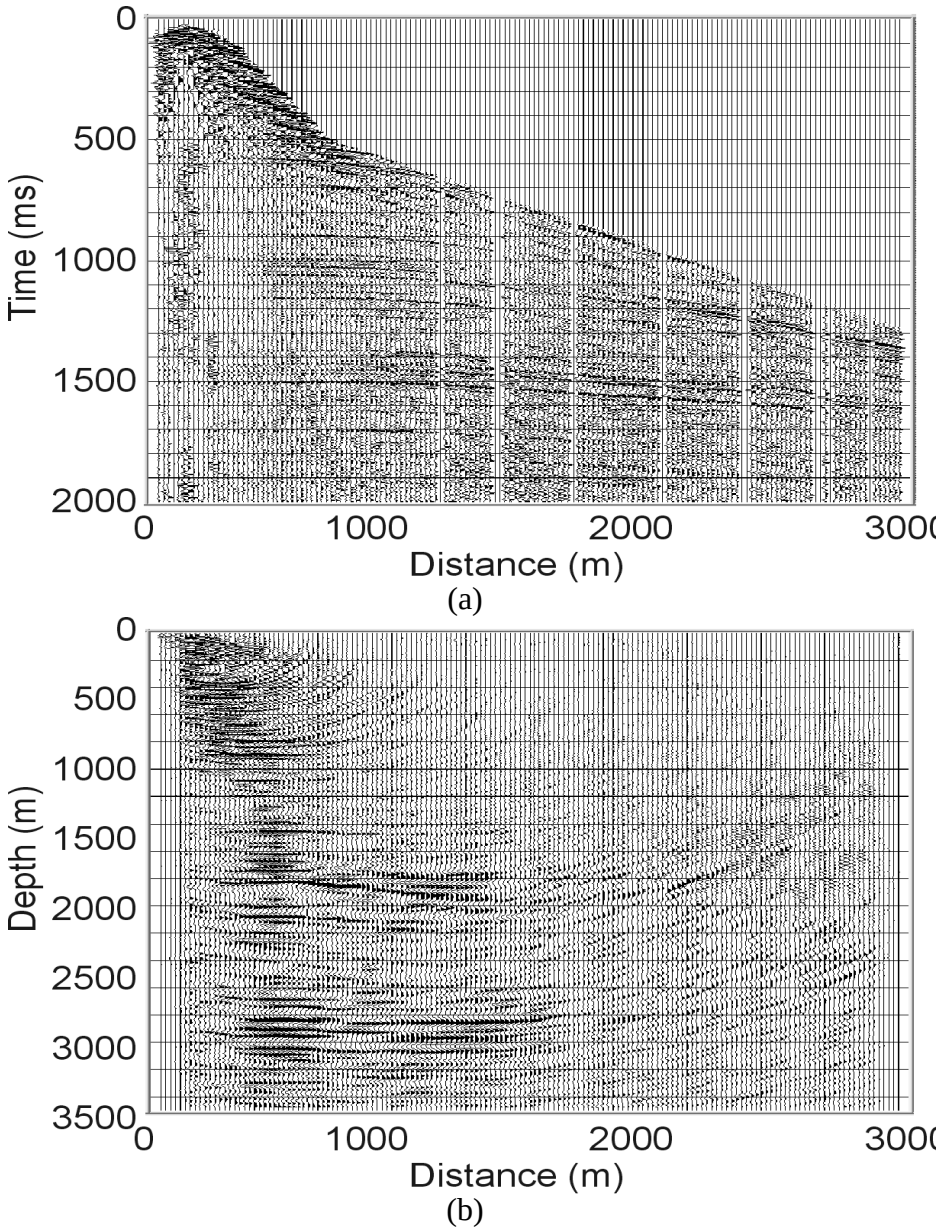

FIG. 14. Vertical component shot gather 10 (a) after the pre-migration processing and (b) after migration.

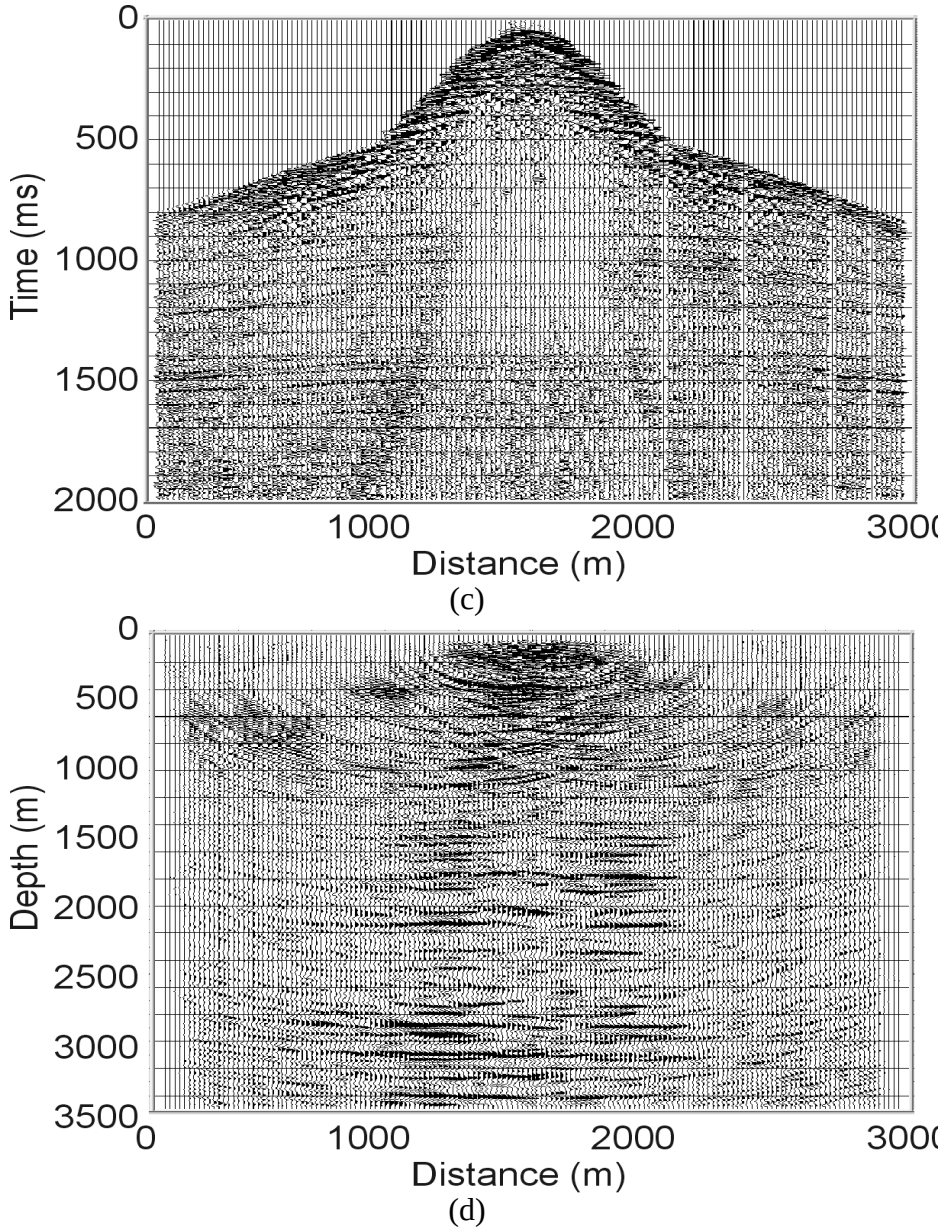

FIG. 14. (continued) Vertical component shot gather 75 (c) after the pre-migration processing and (d) after migration.

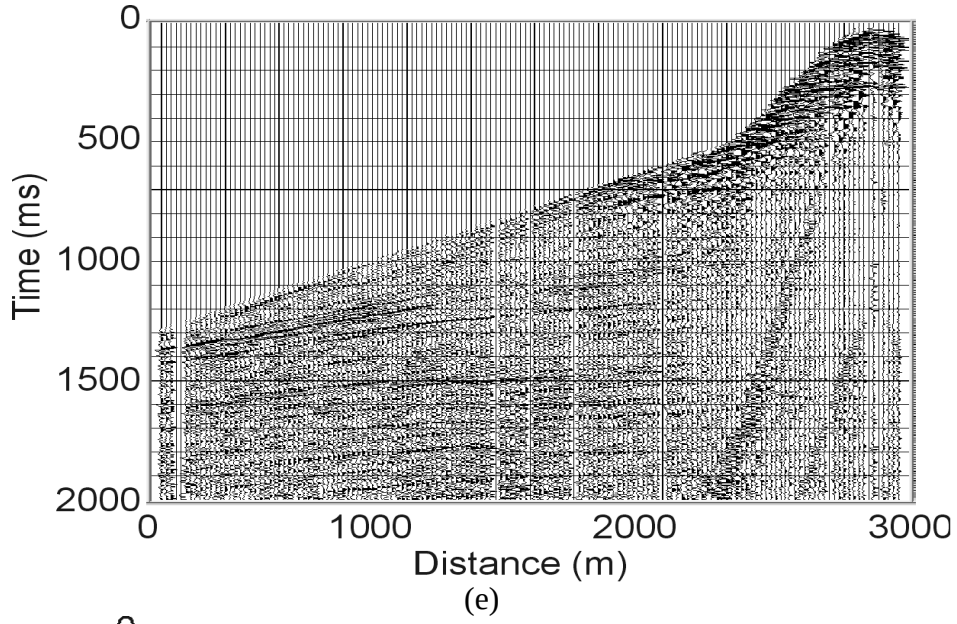

(e)

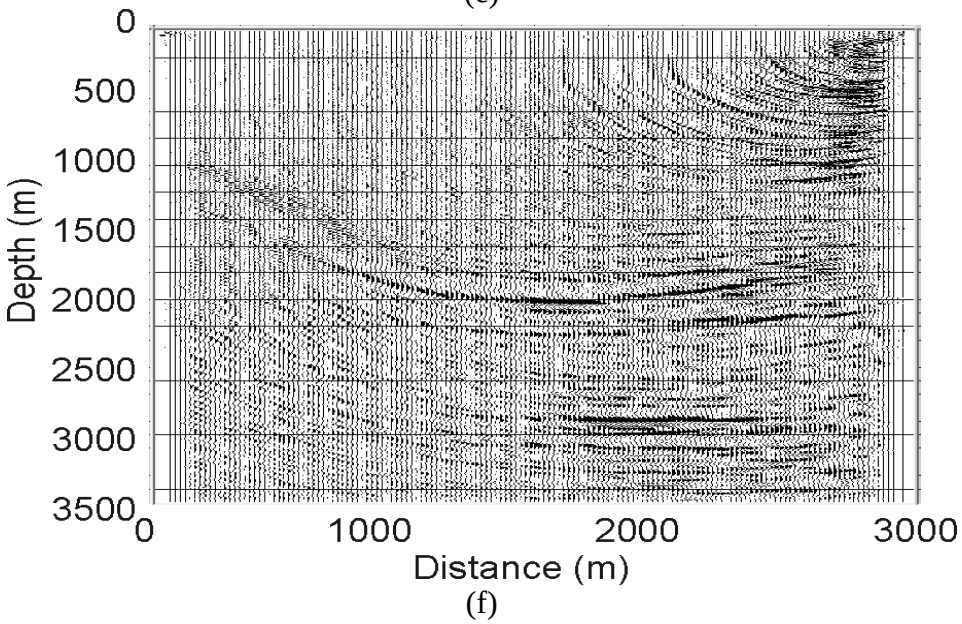

(f)

FIG. 14. (continued) Vertical component shot gather 150 (e) after the pre-migration processing and (f) after migration.

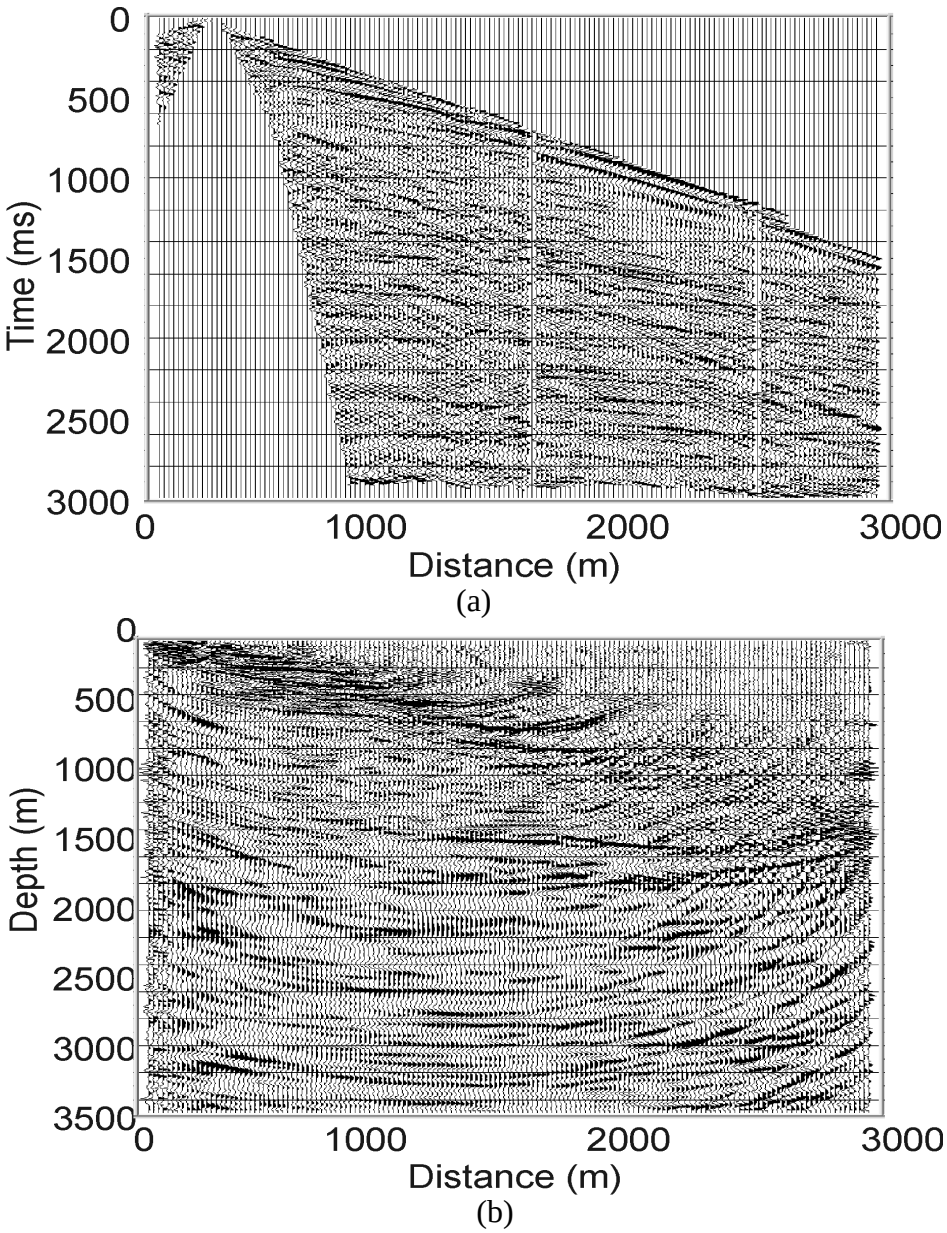

FIG. 15. Radial component shot gather 10 (a) after the pre-migration processing and (b) after migration.

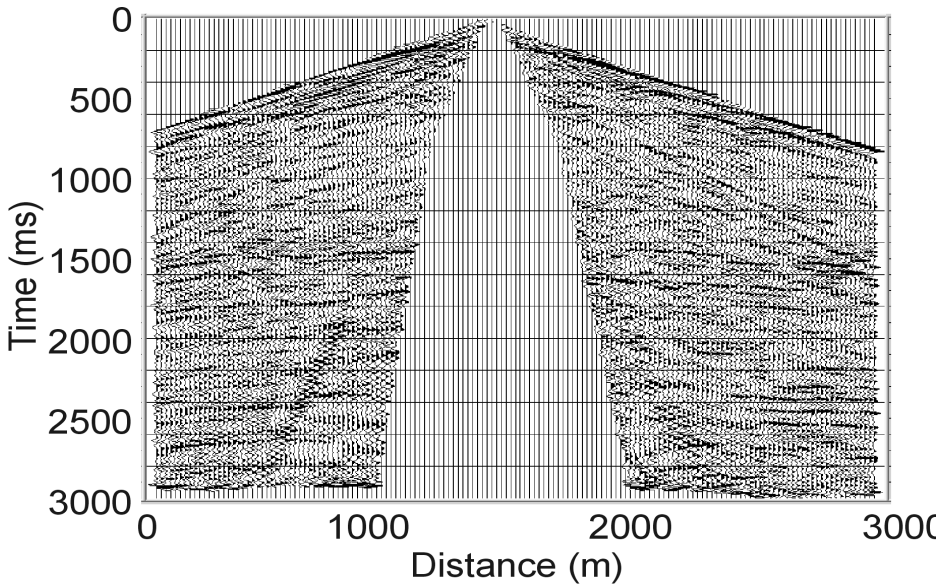

(c)

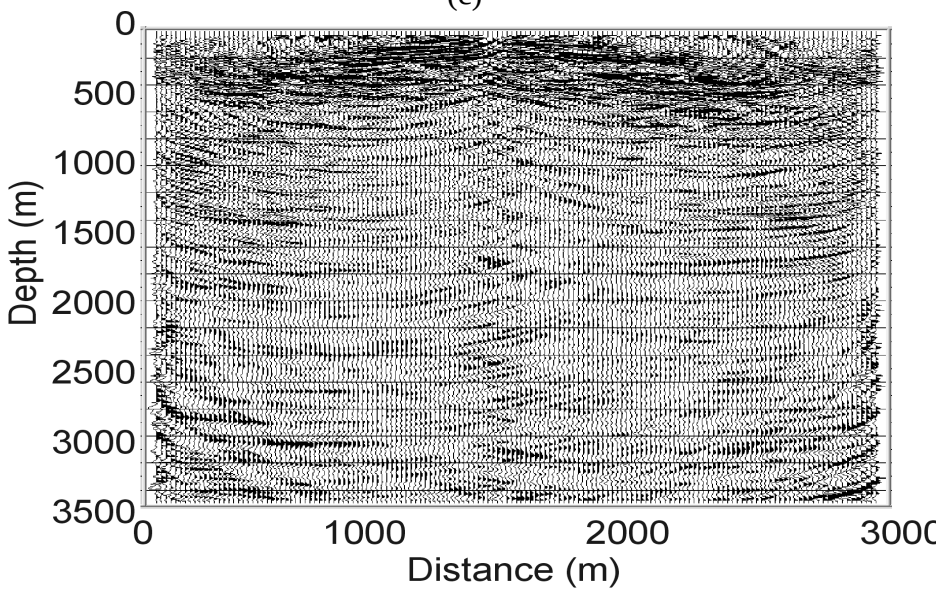

(d)

FIG. 15. (continued) Radial component shot gather 75 (c) after the pre-migration processing and (d) after migration.

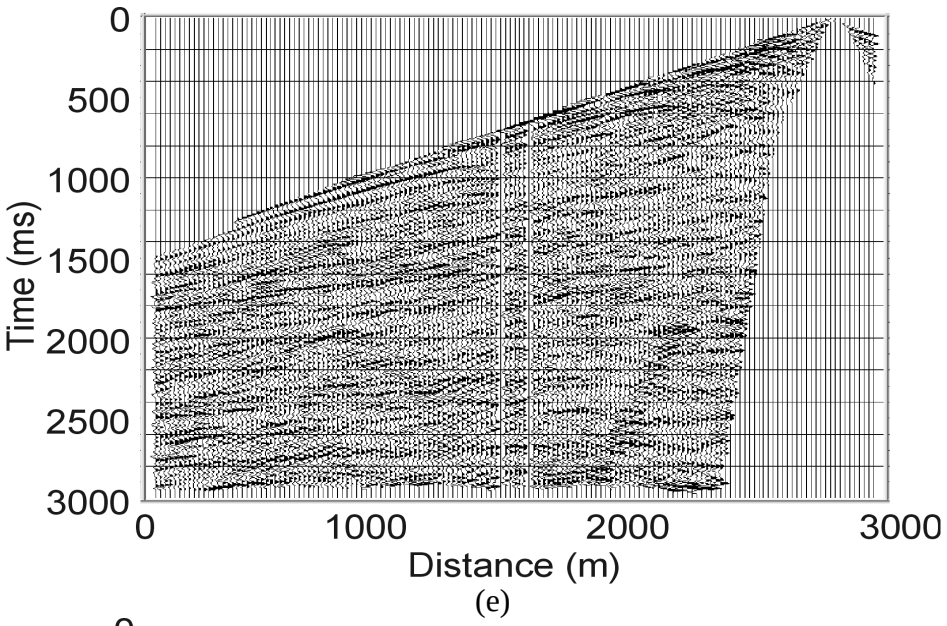

(e)

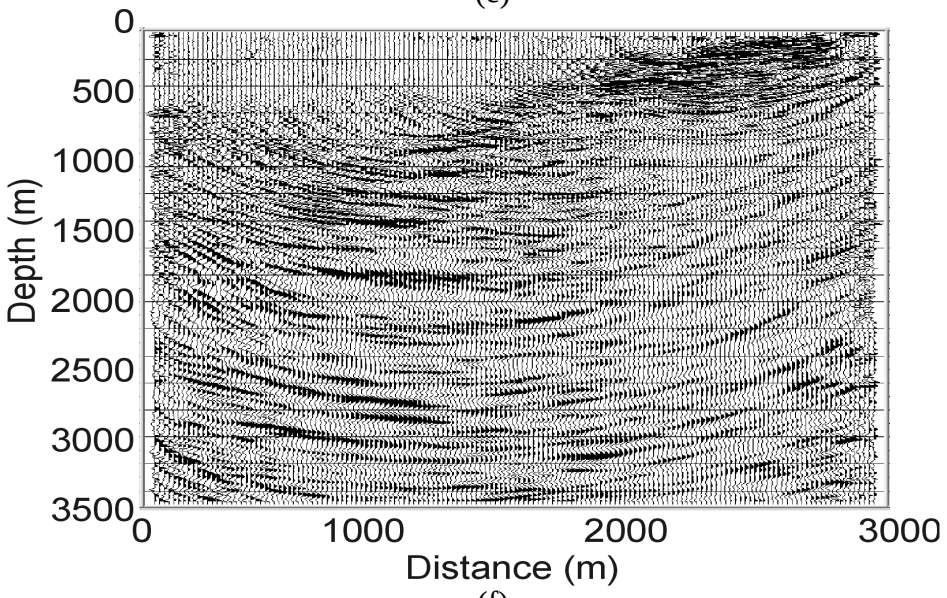

(f)

FIG. 15. (continued) Radial component shot gather 150 (e) after the pre-migration processing and (f) after migration.

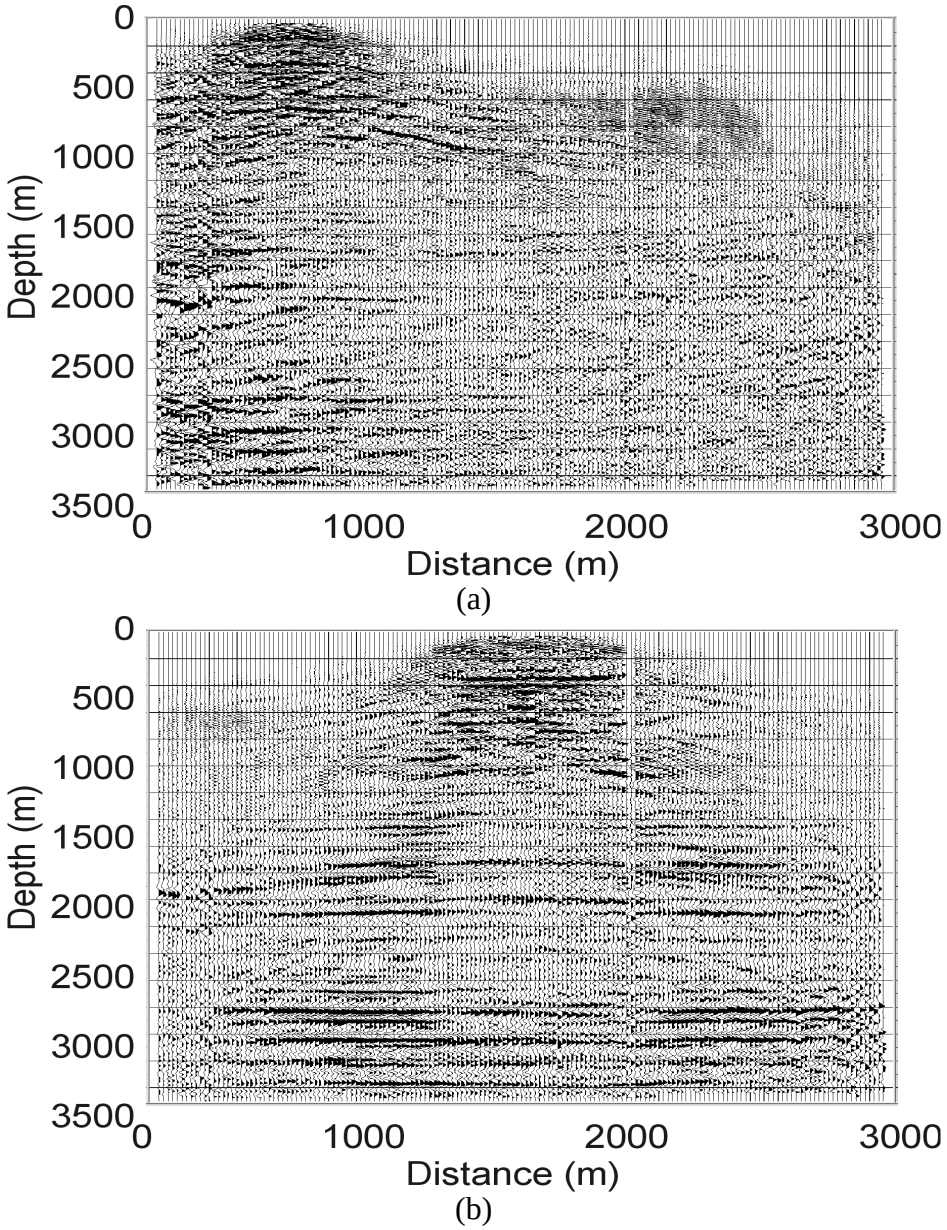

FIG. 16. Vertical-component CIGs located on at 500m, 1500m and 2500m from the left end of the line. (a) CIG at 500m, (d) CIG at 1500m.

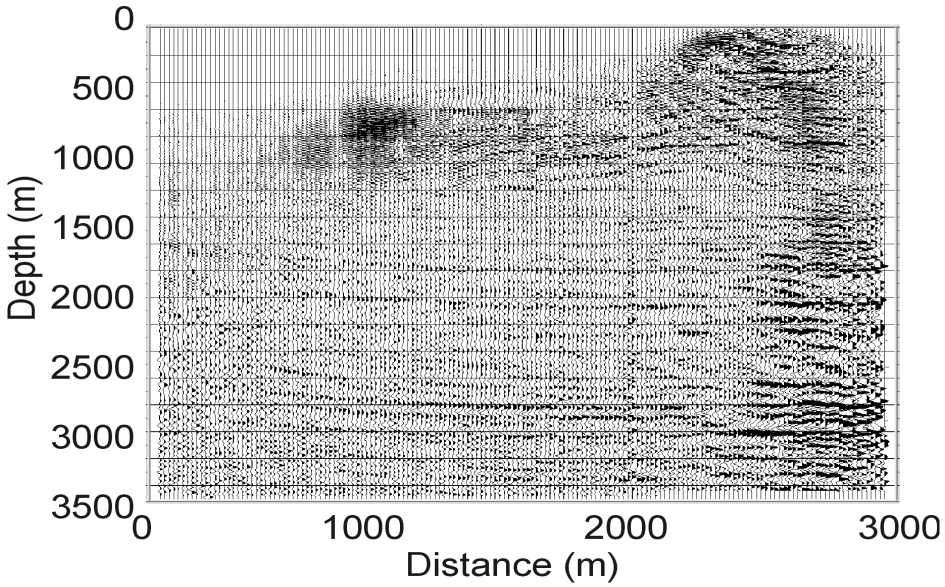

FIG. 16. (continued) Vertical-component CIGs located on at 500m, 1500m and 2500m from the left end of the line. (c) CIG at 2500m.

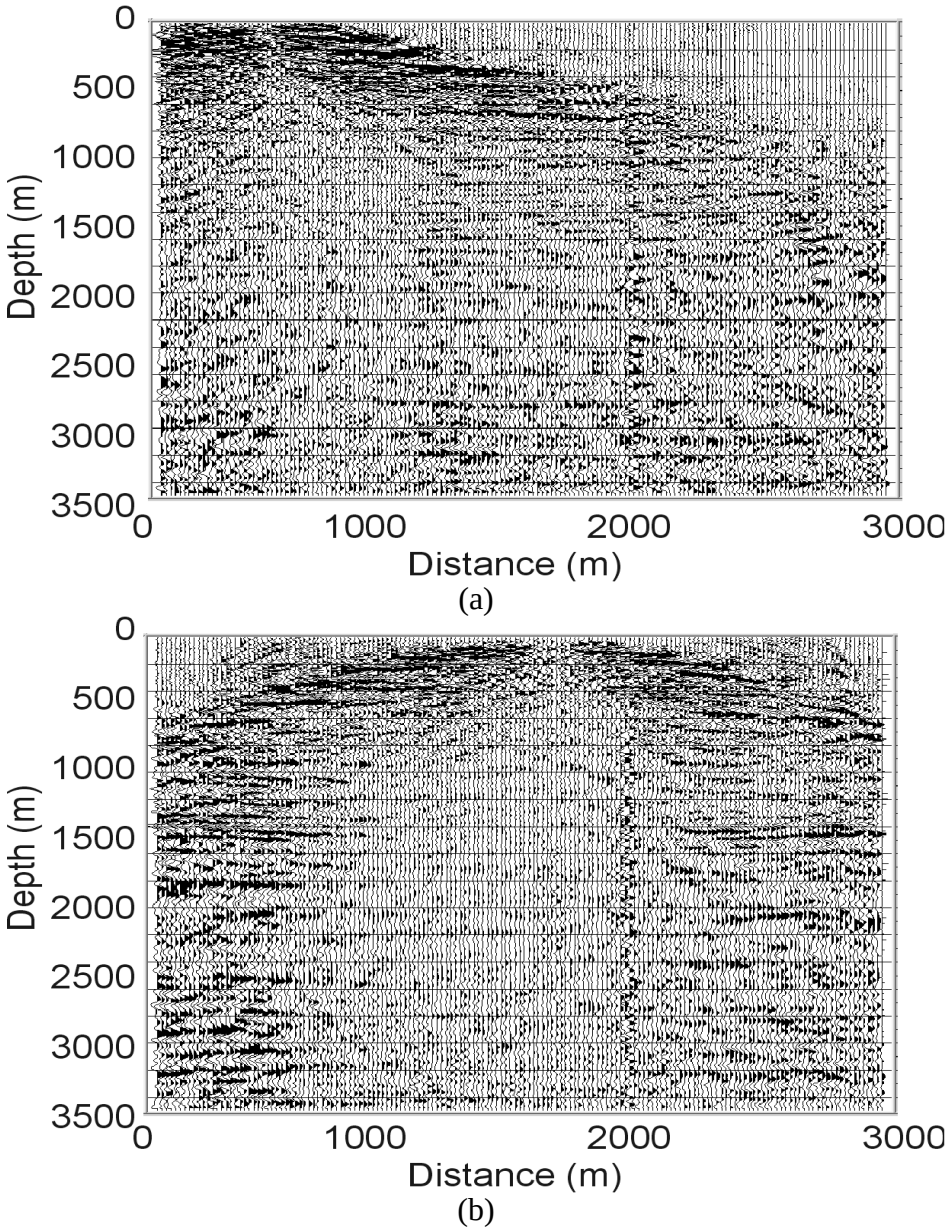

FIG. 17. Three radial-component CIGs located at 500m, 1500m and 2500m. (a) CIG at 500m, (b) CIG at 1500m.

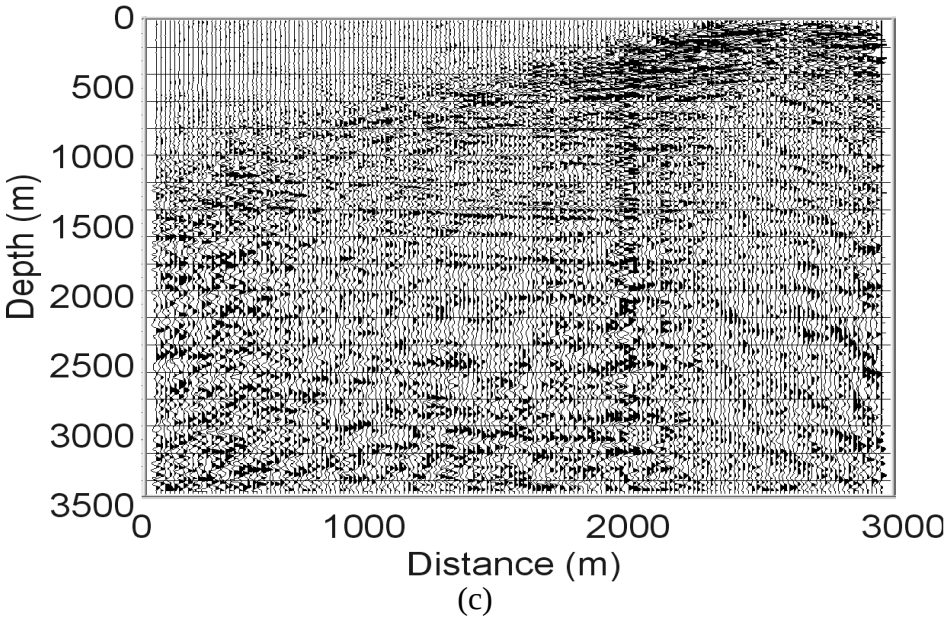

FIG. 17. (continued) Three radial-component CIGs located at 500m, 1500m and 2500m. (a) CIG at 500m, (c) CIG at 2500m.

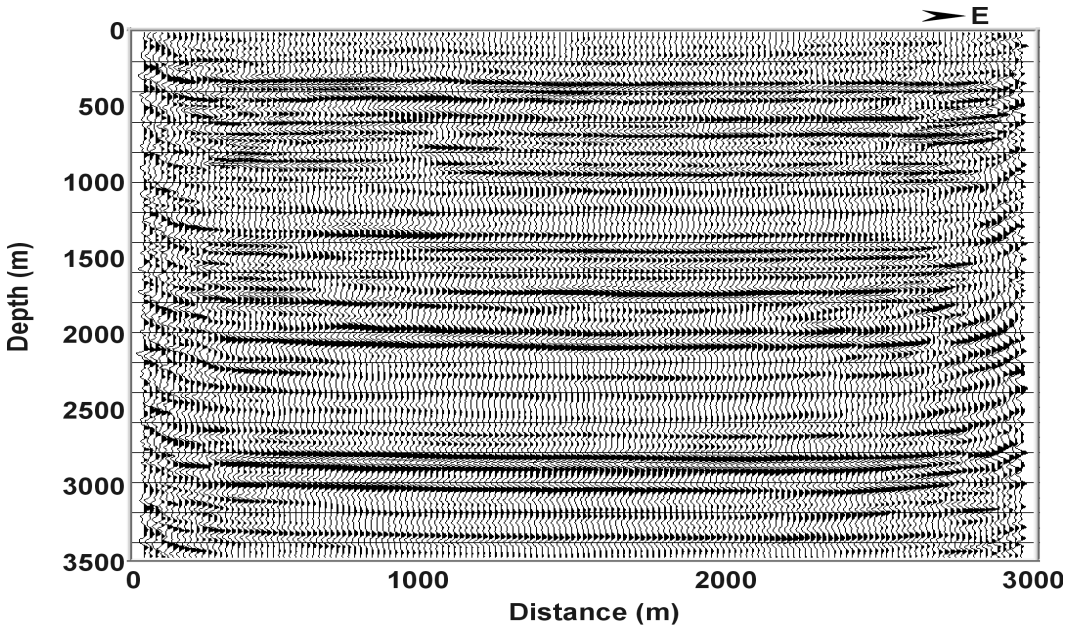

FIG. 18. Vertical component depth image.

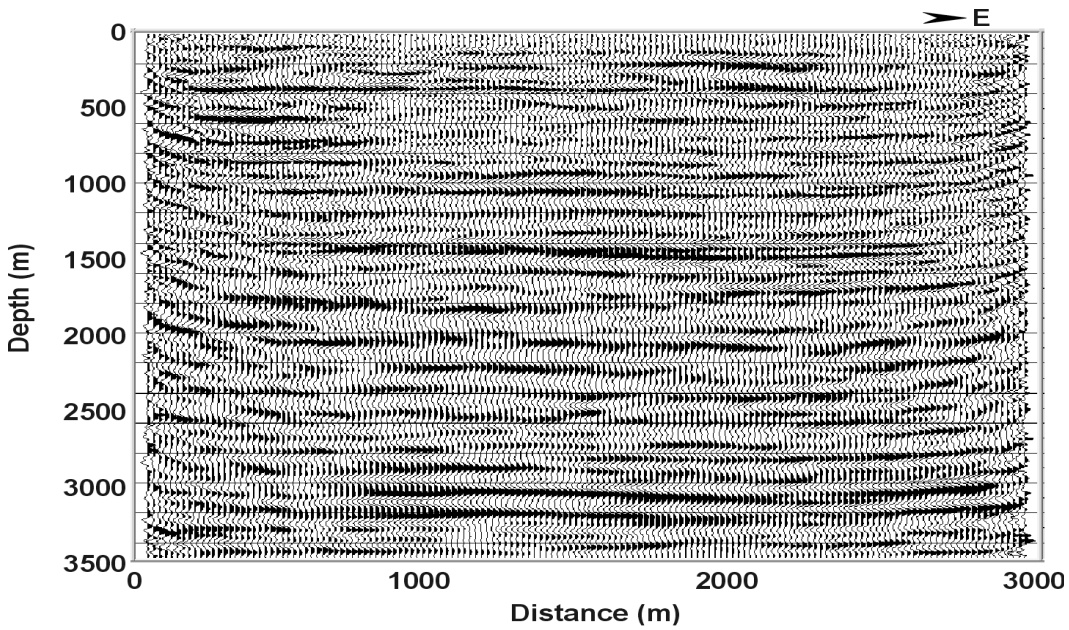

FIG. 19. Radial component depth image.

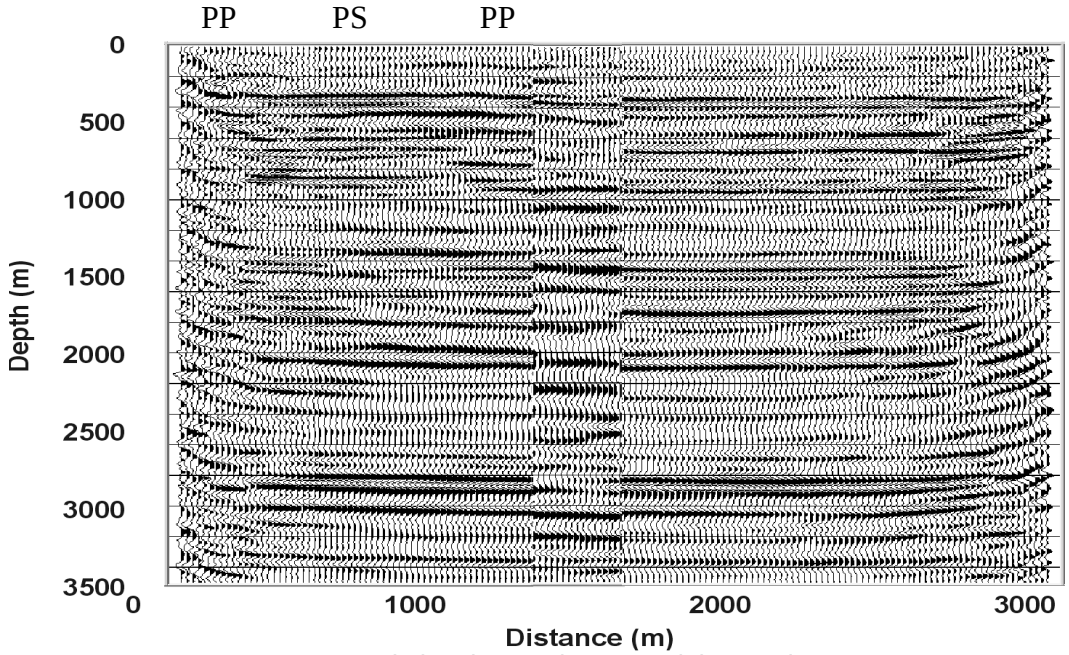

FIG. 20. Correlation the P-P image and the P-S image.